ADVANCED FUNCTIONAL MATERIALS
www.afm-journal.de

Ordered 3D Thin-Shell Nanolattice Materials with Near-Unity Refractive Indices

*Xu A. Zhang, Abhijeet Bagal, Erinn C. Dandley, Junjie Zhao, Christopher J. Oldham, Bae-Ian Wu, Gregory N. Parsons, and Chih-Hao Chang**

The refractive indices of naturally occurring materials are limited, and there exists an index gap between indices of air and available solid materials. With many photonics and electronics applications, there has been considerable effort in creating artificial materials with optical and dielectric properties similar to air while simultaneously being mechanically stable to bear load. Here, a class of ordered nanolattice materials consisting of periodic thin-shell structures with near-unity refractive index and high stiffness is demonstrated. Using a combination of 3D nanolithography and atomic layer deposition, these ordered nanostructured materials have reduced optical scattering and improved mechanical stability compared to existing randomly porous materials. Using ZnO and Al_2O_3 as the building materials, refractive indices from 1.3 down to 1.025 are achieved. The experimental data can be accurately described by Maxwell Garnett effective media theory, which can provide a guide for index design. The demonstrated low-index, low-scattering, and high-stiffness materials can serve as high-quality optical films in multilayer photonic structures, waveguides, resonators, and ultra-low-*k* dielectrics.

1. Introduction

Material refractive index is one of the most fundamental quantities in optics and strongly affects light–matter interactions. Beyond bulk material effects, the contrast of refractive indices between two materials is an essential factor in determining the performance of photonic structures and devices. For example, high index contrast is crucial to achieve wide photonic band gaps in photonic crystals.[1] In distributed Bragg reflectors, index contrast is directly related to the operating bandwidth and penetration depth.[2] Symmetric low-index claddings can help reduce loss in planar waveguides.[3] However, the lowest index in naturally occurring solid materials is found in MgF_2 (n = 1.37), and an index gap exists between that and air (n = 1). Air-bridge type structures using free space as the low-index medium have been demonstrated, but freestanding structures exhibit lower mechanical stability.[4] In addition, the ability to achieve arbitrary refractive index profile is also important in applications such as gradient-index devices and antireflection coatings.[5–8] There is much research interest for mechanically stable artificial materials with arbitrary low indices to completely fill the index gap.

An effective method to lower the material's effective refractive index is to introduce air voids and make the material porous, which can be achieved using various mechanisms. Oblique deposition is an effective technique and has demonstrated random slanted nanorods with low index, achieving a porous SiO_2 thin film with n = 1.05.[6,9,10] Such processes can also be used to create stepwise index profiles for broadband gradient-index antireflection coatings.[6] Other approaches adopt bottom-up techniques, such as sol–gel process for silica aerogel films (n = 1.049),[11] demixing of poly(methy methacrylate) (PMMA) and polystyrene (PS) mixtures (n = 1.05),[12] and chemical vapor deposition of carbon nanotube (CNT) arrays (n = 1.026).[13] These techniques can fill up the aforementioned index gap, and materials with low index have been demonstrated. However, the low-index materials achieved so far have been limited to random structures, resulting in reduced mechanical stability.[14] Random order can also lead to high optical scattering, resulting in the translucent appearance commonly observed in silica aerogels.[15] It can also be difficult to control the nanostructure geometry, limiting precise index design. In addition, many of these materials also have high absorption, which makes them unsuitable for photonic applications.[12,13] In electronics applications, low-*k* dielectrics also require high porosity and mechanical stability, however, only random porous low-*k* materials have been demonstrated.[14,16,17]

Periodic order in porous and cellular structures is desirable when it comes to enhancing mechanical stability at low density. Recent research has demonstrated that mechanical

X. A. Zhang, A. Bagal, Prof. C.-H. Chang
Department of Mechanical and Aerospace Engineering
North Carolina State University
Raleigh, NC 27695, USA
E-mail: chichang@ncsu.edu
E. C. Dandley, J. Zhao, Dr. C. J. Oldham, Prof. G. N. Parsons
Department of Chemical and Bimolecular Engineering
North Carolina State University
Raleigh, NC 27695, USA
Dr. B.-I. Wu
Air Force Research Laboratory
1864 4th Street Wright-Patterson AFB, Dayton, OH 45433, USA

DOI: 10.1002/adfm.201502854

stiffness and yield strength scale more favorably at low densities when the porous structure has periodic as opposed to random architectures.[18–21] Periodic order can also reduce optical scattering, enhance transmission, and enable precise geometry control, leading to the rational design of refractive index. In recent years various 3D nanolithography techniques, such as interference lithography,[22] multiphoton lithography,[23] phase-shift lithography,[24] and colloidal phase lithography,[25–27] have been developed to fabricate ordered porous nanostructures. However, such structures typically have relatively high solid volume fraction near 50%, and require additional processes to reduce material density.

Here, we demonstrate an alternative class of 3D periodic nanolattice materials where their refractive indices can be tuned within the air-gap index range. Using a combination of 3D nanolithography and atomic layer deposition (ALD), the structure geometry and material composition can be controlled to design the material's effective index. In this approach the nanolattice period and unit-cell geometry can be designed by lithography with nanometer-level precision,[27] while the shell thickness can be controlled by ALD with subnanometer accuracy. Compared to random pore arrangements, periodic architecture has improved mechanical stability and reduced light scattering. The periodic geometry can also be accurately designed and modeled using developed analytical and numerical models. Refractive index as low as 1.025 was achieved using Al_2O_3 (bulk index ≈ 1.65) over the visible and near-infrared wavelength range. The fabricated structure has an index smaller than the existing lowest index material ($n \approx 1.05$),[6,9–12] while simultaneously have higher mechanical robustness, lower scattering, and high transparency. Low-density CNT forest has demonstrated indices in the same range ($n = 1.026$), however they have high absorption and are therefore not suitable for certain photonics applications. Higher refractive indices can also be designed by controlling geometry and material composition to completely fill the air-gap index range. The use of ALD on lithographically patterned porous microstructures has been demonstrated as lightweight lattice materials with enhanced mechanical properties,[20,21] and here, we demonstrate it can also be employed to design ultra-low index materials.

The proposed fabrication process is depicted in **Figure 1**, where a periodic 3D photoresist template is first patterned using nanosphere phase lithography.[27] Note other 3D nanolithography techniques[22–24] can also be used to define the 3D template. Conformal thin films of various material compositions were then deposited on the template surface using ALD. In this work, ZnO and Al_2O_3 were selected to fabricate the low-index nanolattice materials for high optical transmission and mechanical stiffness. The polymer core was then removed by a combination of solvent dissolution, thermal treatment, and plasma cleaning, leaving a nanolattice material consisting of periodic thin-shell structures. The nanolattice material volume fraction was controlled by the remaining shell thickness, which can be used to design the material's effective index. This film is then treated as a homogeneous thin film for optical characterization.

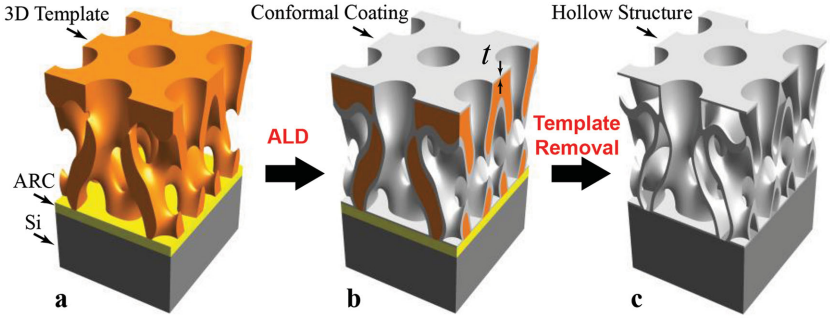

Figure 1. Fabrication process of low-index nanolattice materials with periodic order. a) A 3D polymer template is defined by nanolithography using colloidal particles. Antireflection coating (ARC) is applied to reduce back reflection. b) A conformal coating on the 3D template is achieved by atomic layer deposition with subnanometer thickness precision. c) Polymer template cores are removed, leaving a 3D porous low-index material.

2. Results and Discussion

Fabricated 3D nanolattices are shown in the scanning electron microscope (SEM) images in **Figure 2**. Cross-sectional and top-view SEM micrographs of nanolattices with 6.0 nm Al_2O_3 shells are shown in Figure 2a–c, respectively. Similarly, nanolattices with 19.0 nm thick Al_2O_3 are shown in Figure 2d,e. For both samples, the photoresist templates were fabricated using 325 nm wavelength exposure on a monolayer of close-packed array of polystyrene spheres with diameter $D = 500$ nm. The geometry features a periodic array of tubular nanostructures and secondary shell structures in between. The ordered arrangement of tubular structures can enhance mechanical stiffness, and the 15.0 nm shell Al_2O_3 nanolattice sample with 16.74% solid fraction has achieved a stiffness of ≈7 GPa (for mechanical characterization see Section F in the Supporting Information). Such stiffness would require twice the volume fraction in porous Al_2O_3 aerogel with random architecture.[28] Different pore arrangements and solid volume fractions can be readily achieved by altering particle diameters and lithography exposure parameters.[27] As shown in Figure 2f,g, another polymer core was fabricated using 325 nm wavelength illumination and 390 nm diameter polystyrene spheres. The resultant nanolattices have shorter tubular geometry and more complex periodic structures, denoted as Lattice B. The shell material is ZnO with a 31.8 nm thickness. More samples were fabricated to investigate the index design, as shown in Section E in the Supporting Information.

The broadband optical indices of various Al_2O_3 and ZnO nanolattice materials are plotted in **Figure 3**a,b, respectively. All samples were measured using spectroscopic ellipsometry with Sellmeier model fitting. The indices of air and the film materials are also plotted as reference. The lowest index demonstrated is 1.025 for the Al_2O_3 nanolattices with 2.1 nm thick shells (solid fraction, $f = 2.63\%$), as shown in Figure 3a, compared with $n \approx 1.65$ for bulk Al_2O_3. The refractive index increases with increasing shell thickness as expected, and the material dispersion becomes more pronounced. For lower shell thickness values the index is nearly constant,

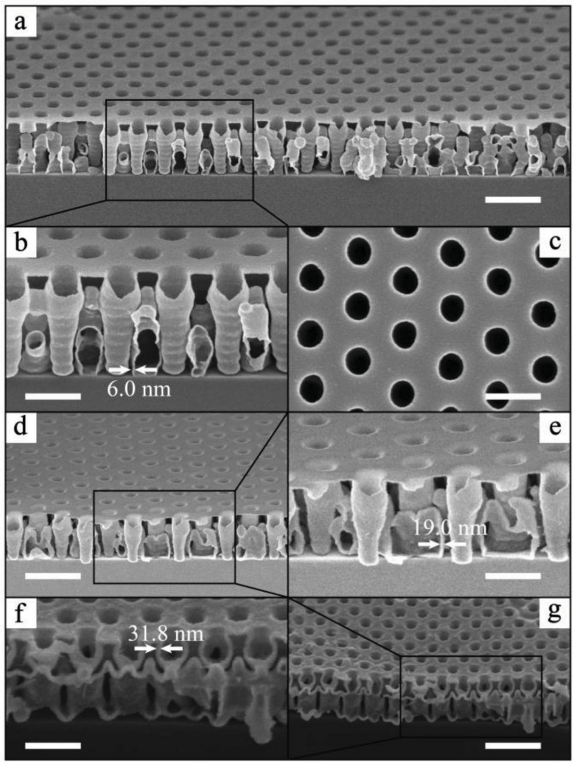

Figure 2. Scanning electron micrographs of various low-index nanolattice materials. a–c) Cross sections and top views of low-index materials with 6.0 nm thick Al_2O_3 shells. Geometry was defined using 500 nm polystyrene spheres and 325 nm wavelength laser. d,e) Cross sections of low-index materials have the same template geometry with 19.0 nm Al_2O_3 shell thickness. f,g) Cross sections of low-index materials with 31.8 nm thick ZnO shells. The geometry (Lattice B) is different, fabricated using 390 nm polystyrene spheres and 325 nm wavelength laser. Scale bars represent 1 μm in panels (a), (d), and (g), and 500 nm in panels (b), (c), (e), and (f).

as exemplified by the 2.1 and 6.0 nm samples (for raw index data and fitting parameters, see Section C in the Supporting Information). The colored regions in Figure 3a,b indicate the predicted upper and lower bounds for the 19.0 nm Al_2O_3 and 21.3 nm ZnO nanolattices, respectively, as governed by rules of mixtures.[29a] The solid volume fractions for these Al_2O_3 samples range from 2.63% to 21.97%, and the index is tuned from 1.025 to 1.111 at 633 nm wavelength. The same methodology is applied to the ZnO samples with volume fractions from 27.41% to 36.75%, as shown in Figure 3b, tuning the index from 1.216 to 1.343 at 633 nm wavelength. The ZnO samples generally have thicker shells compared to Al_2O_3 samples, since the polycrystalline ZnO film becomes porous at low thickness and is more susceptible to crack formation. In addition to thicker shells, ZnO also has a higher bulk index, which leads to higher index values for ZnO nanolattice samples. The index variation for different unit-cell lattices can be attributed to varying surface areas, which results in different volume fractions, as indicated by the sample with Lattice B geometry. The material difference in the nanolattices facilitates continuous index variation from 1.025 to 1.360, which fills the index gap for naturally occurring solid materials. The nanolattice materials also exhibit slight material anisotropy, which is discussed further in Section D in the Supporting Information.

It is crucial to have the ability to predict the index value for a given nanolattice and enable inverse design of geometry for a target index. For all the fabricated samples in this work, the Maxwell Garnett effective media model can be used to relate solid volume fraction with the material properties.[29b–31] The Maxwell Garnett equation for nonmagnetic dielectric materials can be rearranged as

$$\frac{\frac{n_{\text{eff}}^2-1}{n_{\text{eff}}^2+2}}{\frac{n_{\text{m}}^2-1}{n_{\text{m}}^2+2}} = f \tag{1}$$

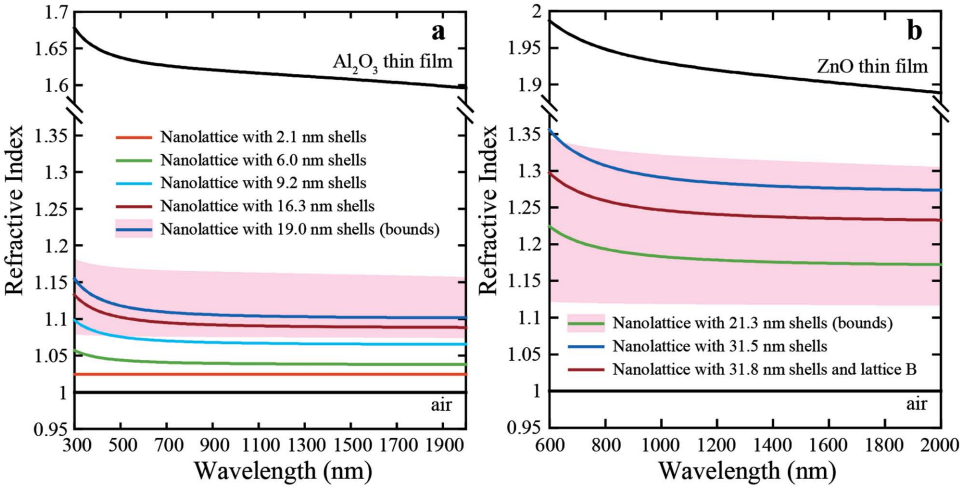

Figure 3. Measured broadband refractive indices for various nanolattices with different material composition and shell thicknesses. a) Index of Al_2O_3 samples with different thicknesses. Colored region shows the index bounds for 19.0 nm lattice using first-order effective medium approximation. b) Index of ZnO samples with different thicknesses. Colored region shows the index bounds for 21.3 nm lattice using first-order effective medium approximation.

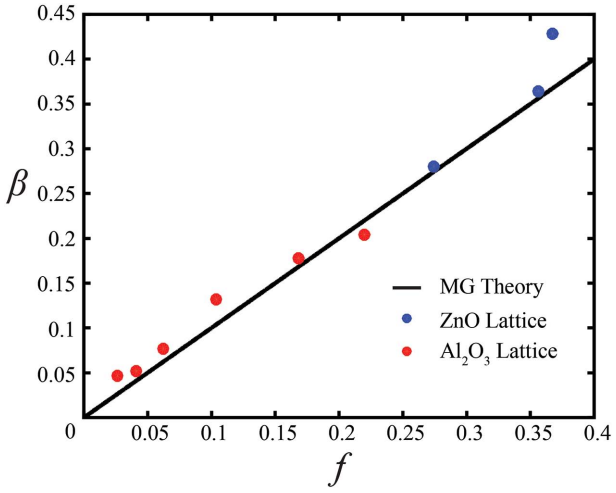

Figure 4. Normalized material property, β, versus solid volume fraction, f. The analytical model plotted is based on Maxwell Garnett effective medium theory. The experimental data are indices at 633 nm wavelength for all the samples.

where n_{eff} is the effective index of the nanolattice material, n_{m} is the index of the constituent material, and f is the solid volume fraction. Setting $\beta = \left(\frac{n_{\text{eff}}^2 - 1}{n_{\text{eff}}^2 + 2}\right) / \left(\frac{n_{\text{m}}^2 - 1}{n_{\text{m}}^2 + 2}\right)$ as a unitless parameter normalized to the shell material, a simple linear relationship to volume fraction can be found, $\beta = f$. For the convenience of discussion, we chose the index values at 633 nm wavelength for all samples and plotted them with the Maxwell Garnett model, as shown in **Figure 4**, but this relationship holds for all wavelengths. The data fits the analytical model well, indicating a linear relationship between the normalized indices and volume fraction. Note that Maxwell Garnett model is not suitable for binary mixtures with comparable volume fractions,[31] therefore our analysis is limited to 40% solid volume fraction. This simple effective media model serves as a convenient guide for the index prediction and lattice geometry/material design. For example one may calculate the desired volume fraction given a constituent material and a target index, which can then be achieved using the proposed nanolithography and ALD processes. Note that the design and prediction capabilities are enabled by the precise geometry and material control demonstrated in this work.

Beyond effective index design and mechanical robustness, another advantage of ordered nanostructures is low light scattering, which is a crucial requirement for high-quality optical films. The specular and diffused scattering transmissions of the nanolattice materials were characterized using a spectrophotometer with an integrating sphere, as depicted in **Figure 5**a. The transmission of glass is included as reference. The nanolattice materials with 15.2 and 20.3 nm shells on glass samples show slight thin-film interference effects, which leads to enhanced transmission in certain wavelength ranges. The scattering of the nanolattice material is generally low in the visible and near-infrared range but peaks to around 6% at around 320 nm.

The major source of scattered light is diffraction due to the ordered honeycomb lattice geometry, as observed in the diffraction ring shown in the inset of Figure 5. Here, the sample was illuminated by a 325 nm wavelength laser. The circular diffraction pattern captured on a fluorescent screen indicates a locally periodic structure lacking long-range order due to assembly defects. The average lattice spacing can be determined from the ring radius, and is calculated to be around 435 nm. This agrees well with the lithography configuration, where the lattice period is given by $\Lambda = D\sqrt{3}/2$. Such diffraction effects can be eliminated by further reducing the nanolattice period, and is evident in the low scattering measured beyond 500 nm. The diffraction effect can also be seen in the scattering angular profiles, as shown in the inset diagram. Here, it can be observed that for 325 nm scattering a peak exists at around 48°, corresponding to the diffraction ring radius, while the 633 nm scattering decreases monotonically. It is important to note that for both of these cases the scattering angular profile is very different from Rayleigh scattering seen in random porous materials, where scattering is independent of angle. Such angle-independent scattering leads to hazy and translucent appearance, which is suppressed in the fabricated samples shown in Figure 5b. Here,

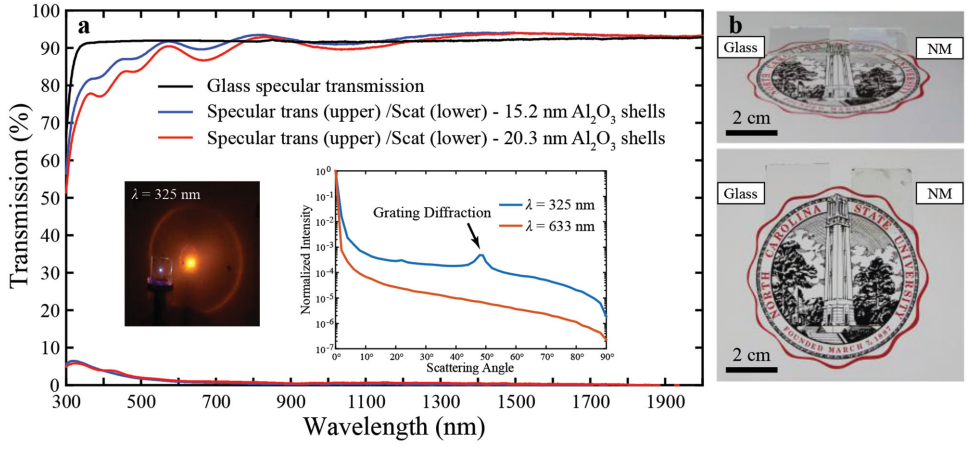

Figure 5. a) Specular transmission and light scattering properties of the fabricated low-index nanolattice materials. The specular transmission of glass is plotted for comparison. b) Photographs of fabricated sample and bare glass. "NM" is the nanolattice material with 15.2 nm Al_2O_3 shells. A tablet screen was used as a backlit background.

a nanolattice sample is placed next to a bare glass slide, and both samples visually exhibit broadband clarity. Note at oblique observation angles the nanolattice sample has a slight color due to thin-film interference effects.

Beyond diffraction effects, particle assembly defects during the lithography step can also introduce lattice imperfection and contribute to scattering in the ultraviolet region. This can be improved by using a perfectly periodic 3D template with long-range order or other nanolithography approaches. In addition, structural collapse of the thin-shell nanolattice can also result in local defects and induce scattering. This can be further reduced by better control of processing conditions and uniformity. Note that while the materials used are limited to ZnO and Al_2O_3, any materials that can be coated using ALD are compatible with this process. The packaging and integration of these materials into photonic devices is currently under study.

3. Conclusion

In conclusion, we demonstrate a new class of low-index nanolattice materials consisting of ordered thin-shelled structures that have a near-unity index. The refractive index can be designed by controlling lattice geometry using nanolithography and selecting material composition and thickness during ALD. The index can be varied by a wide range, $n = 1.025$ to 1.360, to completely fill the index gap between naturally occurring solid materials and air. The experimental results were well-modeled using Maxwell Garnett effective medium theory, which can be used to guide index design. Light scattering of the nanolattice materials are low in the visible and near-infrared range, and the angle-dependent scattering profile results in a reduced translucent appearance. Lower scattering in the UV range can be achieved by further reducing the lattice period and minimizing structure defects. The developed low-index films can find many applications in waveguides, resonators, photonic devices, and low-*k* dielectric materials.

4. Experimental Section

Nanolattice Materials Fabrication: In all experiments, the polymer template was fabricated using positive photoresist (Sumitomo PFi88A7). An antireflection layer (ARC i-CON-16, Brewer Science, Inc.) was used under the resist to reduce back reflection. Silicon and glass substrates were used for refractive index and transmission measurements, respectively. A HeCd laser with 325 nm wavelength was used for exposure to make photoresist template. Close-packed monolayers of polystyrene nanospheres with diameters of 390 nm (1% particle size standard, Bangs Laboratories, Inc.) and 500 nm (2.5% Polybead Nonfunctionalized Microspheres, Polysciences, Inc.) were used as phase masks. Lattice B geometry is referred to the nanolattice materials fabricated from 390 nm spheres.

Photoresist nanostructure templates were subsequently coated with ZnO or Al_2O_3 using ALD in a custom made viscous-flow, hot-walled, vacuum reactor described previously.[32–34] ALD consists of two, self-limiting half reactions that produce a conformal thin film on samples of interest. Supplies were purchased commercially and used as received. The reactor was purged with high purity nitrogen gas (Machine & Welding Supply Co) that was further purified with an Entegris GateKeeper. Trimethyl aluminum (TMA, Strem Chemicals, min 98% pure) was used as a precursor and coreacted with deionized water to deposit Al_2O_3. The ALD recipe used for these experiments was 1/30/1/60 (TMA dose/nitrogen purge/water dose/nitrogen purge, in seconds) with a typical growth rate of 1.1 Å per cycle. The reactor was kept around 550 mTorr at 90 °C. Diethyl zinc (DEZ, Strem Chemicals, min 98% pure) was used as the metal-containing precursor for ZnO. DEZ/Water ALD cycles were used for ZnO deposition with growth rate of about 1.6 Å per cycle. In both cases, silicon substrates (University Wafers, P-type, ⟨100⟩) were placed in the front and back of the reactor chamber as monitors for film growth and film thickness was determined using an α-SE ellipsometer (J. A. Woollam Co., Inc).

The polymer template was removed by combinations of thermal treatment using a furnace (Vulcan 3-130, 100-120V, DENTSPLY), solvent dissolution using *N*-Methyl-2-pyrrolidone (NMP), and isotropic oxygen plasma etching (March Instrument PM-600). For thermal treatments, samples were placed in the furnace at room temperature and the temperature was increased to 550 °C, with a ramp rate of 0.3 °C min^{-1}. The temperature was maintained at 550 °C for 30 min to ensure that both the photoresist template and the underlying ARC layer were burned off. The thermal method was used for nanolattice materials with shell thicknesses larger than 10 nm without systematic collapse. For shell thicknesses less than 10 nm of Al_2O_3, the sample was immersed in NMP for 48 h to dissolve the photoresist template. The ARC layer was then removed using the thermal treatment described earlier. Oxygen plasma treatments can also be used for thinner-shelled samples to remove photoresist cores. The samples were etched under 300 W power, 600 mTorr pressure, and 80 sccm flow rate for about 9 h.

Characterizations and Modeling: Refractive index measurements were performed using spectroscopic ellipsometer (J. A. Woollam, V-VASE) over the wavelength range of 400–2000 nm and various incident angles. Sellmeier model was used for all data fittings (for details on ellipsometric modeling, see Section A in the Supporting Information). Transmission and light scattering properties were characterized by a UV–Vis–NIR spectrophotometer (Agilent Cary 5000) with an integrating sphere in transmission mode, according to ASTM D1003-13. Finite-difference time-domain (FDTD) simulation (using MEEP)[35] and a binary resist model were developed to calculate solid volume fraction (details are provided in Section B in the Supporting Information).

Supporting Information

Supporting Information is available from the Wiley Online Library or from the author.

Acknowledgements

The authors gratefully acknowledge the students, staff, and facility support from the North Carolina State University Nanofabrication Facility (NNF), Analytical Instrumentation Facility (AIF), and the Chapel Hill Analytical and Nanofabrication Laboratory (CHANL) at the University of North Carolina at Chapel Hill. AIF is located at North Carolina State University and is supported by the State of North Carolina and the National Science Foundation. This work was supported by a NASA Office of the Chief Technologist's Space Technology Research Opportunity–Early Career Faculty Grant (Grant No. NNX12AQ46G) and Air Force Research Laboratory.

Received: July 10, 2015
Revised: September 7, 2015
Published online: October 12, 2015

[1] B. Temelkuran, S. D. Hart, G. Benoit, J. D. Joannopoulos, Y. Fink, *Nature* **2002**, *420*, 650.
[2] S.-T. Ho, S. L. McCall, R. E. Slusher, L. N. Pfeiffer, K. W. West, A. F. J. Levi, G. E. Blonder, J. L. Jewell, *Appl. Phys. Lett.* **1990**, *57*, 1387.

[3] M. Schmidt, G. Boettger, M. Eich, W. Morgenroth, U. Huebner, R. Boucher, H. G. Meyer, D. Konjhodzic, H. Bretinger, F. Marlow, *Appl. Phys. Lett.* **2004**, *85*, 16.
[4] C. Marinelli, M. Bordovsky, L. J. Sargent, M. Gioannini, J. M. Rorison, R. V. Penty, I. H. White, P. J. Heard, M. Benyoucef, M. Kuball, G. Hasnain, T. Takeuchi, R. P. Schneider, *Appl. Phys. Lett.* **2001**, *79*, 4076.
[5] S. Chattopadhyay, Y. F. Huang, Y. J. Jen, A. Ganguly, K. H. Chen, L. C. Chen, *Mater. Sci. Eng. R Rep.* **2010**, *69*, 1.
[6] J.-Q. Xi, M. F. Schubert, J. K. Kim, E. F. Schubert, M. Chen, S.-Y. Lin, W. Liu, J. A. Smart, *Nat. Photon.* **2007**, *1*, 176.
[7] C.-H. Chang, J. A. Dominguez-Caballero, H. J. Choi, G. Barbastathis, *Opt. Lett.* **2011**, *36*, 2354.
[8] K.-C. Park, H. J. Choi, C.-H. Chang, R. E. Cohen, G. H. McKinley, G. Barbastathis, *ACS Nano* **2012**, *6*, 3789.
[9] J.-Q. Xi, J. K. Kim, E. F. Schubert, *Nano Lett.* **2005**, *5*, 1385.
[10] J.-Q. Xi, J. K. Kim, E. F. Schubert, D. Ye, T.-M. Lu, S.-Y. Lin, J. S. Juneja, *Opt. Lett.* **2006**, *31*, 601.
[11] N. Kawakami, Y. Fukumoto, T. Kinoshita, K. Suzuki, K. Inoue, *Jpn. J. Appl. Phys.* **2000**, *39*, L182.
[12] S. Walheim, E. Schäffer, J. Mlynek, U. Steiner, *Science* **1999**, *283*, 520.
[13] Z.-P. Yang, L. Ci, J. A. Bur, S.-Y. Lin, P. M. Ajayan, *Nano Lett.* **2008**, *8*, 446.
[14] D. Shamiryan, T. Abell, F. Iacopi, K. Maex, *Mater. Today* **2004**, *7*, 34.
[15] W. J. Platzer, M. Bergkvist, *Sol. Energ. Mater. Sol. C* **1993**, *31*, 243.
[16] A. Jain, S. Rogojevic, S. Ponoth, N. Agarwal, I. Matthew, W. N. Gill, P. Persans, M. Tomozawa, J. L. Plawsky, E. Simonyi, *Thin Solid Films* **2001**, *398*, 513.
[17] M. R. Baklanov, K. Maex, *Philos. Trans. R. Soc. Lond. A Math. Phys. Eng. Sci.* **2006**, *364*, 201.
[18] J.-H. Lee, L. Wang, S. Kooi, M. C. Boyce, E. L. Thomas, *Nano Lett.* **2010**, *10*, 2592.
[19] T. A. Schaedler, A. J. Jacobsen, A. Torrents, A. E. Sorensen, J. Lian, J. R. Greer, L. Valdevit, W. B. Carter, *Science* **2011**, *334*, 962.
[20] L. R. Meza, S. Das, J. R. Greer, *Science* **2014**, *345*, 1322.
[21] X. Zheng, H. Lee, T. H. Weisgraber, M. Shusteff, J. DeOtte, E. B. Duoss, J. D. Kuntz, M. M. Biener, Q. Ge, J. A. Jackson, S. O. Kucheyev, N. X. Fang, C. M. Spadaccini, *Science* **2014**, *344*, 1373.
[22] J.-H. Jang, C. K. Ullal, M. Maldovan, T. Gorishnyy, S. Kooi, C. Koh, E. L. Thomas, *Adv. Funct. Mater.* **2007**, *17*, 3027.
[23] W. Haske, V. W. Chen, J. M. Hales, W. Dong, S. Barlow, S. R. Marder, J. W. Perry, *Opt. Express* **2007**, *15*, 3426.
[24] S. Jeon, J.-U. Park, R. Cirelli, S. Yang, C. E. Heitzman, P. V. Braun, P. J. A. Kenis, J. A. Rogers, *Proc. Natl. Acad. Sci. USA* **2004**, *101*, 12428.
[25] X. A. Zhang, J. Elek, C.-H. Chang, *ACS Nano* **2013**, *7*, 6212.
[26] X. A. Zhang, B. Dai, Z. Xu, C.-H. Chang, *Small* **2015**, *11*, 1285.
[27] C.-H. Chang, L. Tian, W. R. Hesse, H. Gao, H. J. Choi, J.-G. Kim, M. Siddiqui, G. Barbastathis, *Nano Lett.* **2011**, *11*, 2533.
[28] R. Yokokawa, J.-A. Paik, B. Dunn, N. Kitazawa, H. Kotera, C.-J. Kim, *J. Micromech. Microeng.* **2004**, *14*, 681.
[29] a) H. Fujiwara, *Spectroscopic Ellipsometry: Principles and Applications*, Wiley, Chichester, UK **2007**; b) J. C. M. Garnett, *Philos. Trans. R. Soc. Lond. A Math. Phys. Eng. Sci.* **1904**, *203*, 385.
[30] N. J. Hutchinson, T. Coquil, A. Navid, L. Pilon, *Thin Solid Films* **2010**, *518*, 2141.
[31] P. Sarafis, A. G. Nassiopoulou, *Nanoscale Res. Lett.* **2014**, *9*, 1.
[32] J. C. Spagnola, B. Gong, S. A. Arvidson, J. S. Jur, S. A. Khan, G. N. Parsons, *J. Mater. Chem.* **2010**, *20*, 4213.
[33] J. S. Jur, J. C. Spagnola, K. Lee, B. Gong, Q. Peng, G. N. Parsons, *Langmuir* **2010**, *26*, 8239.
[34] B. Gong, Q. Peng, J. S. Jur, C. K. Devine, K. Lee, G. N. Parsons, *Chem. Mater.* **2011**, *23*, 3476.
[35] A. F. Oskooi, D. Roundy, M. Ibanescu, P. Bermel, J. D. Joannopoulos, S. G. Johnson, *Comput. Phys. Commun.* **2010**, *181*, 687.